

Analysis on reservoir activation with the nonlinearity harnessed from solution-processed MoS₂ devices

Authors

Songwei Liu¹, Yang Liu^{1,2}, Yingyi Wen¹, Jingfang Pei¹, Pengyu Liu¹, Lekai Song¹, Xiaoyue Fan³, Wenchen Yang³, Danmei Pan⁴, Teng Ma⁵, Yue Lin⁴, Gang Wang³, Guohua Hu^{1,*}

Affiliations

¹Department of Electronic Engineering, The Chinese University of Hong Kong, Shatin, N. T., Hong Kong S. A. R., China

²Shun Hing Institute of Advanced Engineering, The Chinese University of Hong Kong, Shatin, N. T., Hong Kong SAR, 999077 China

³Centre for Quantum Physics, Key Laboratory of Advanced Optoelectronic Quantum Architecture and Measurement (MOE), School of Physics, Beijing Institute of Technology, Beijing 100081, China

⁴CAS Key Laboratory of Design and Assembly of Functional Nanostructures, and State Key Laboratory of Structural Chemistry, Fujian Institute of Research on the Structure of Matter, Chinese Academy of Sciences, Fuzhou, Fujian 350002, China

⁵Department of Applied Physics, Hong Kong Polytechnic University, Hung Hom, Kowloon, Hong Kong S. A. R., China

*Correspondence to: ghhu@ee.cuhk.edu.hk

Abstract

Reservoir computing is a recurrent neural network that has been applied across various domains in machine learning. The implementation of reservoir computing, however, often demands heavy computations for activating the reservoir. Configuring physical reservoir networks and harnessing the nonlinearity from the underlying devices for activation is an emergent solution to address the computational challenge. Herein, we analyze the feasibility of employing the nonlinearity from solution-processed molybdenum disulfide (MoS₂) devices for reservoir activation. The devices, fabricated using liquid-phase exfoliated MoS₂, exhibit a high-order nonlinearity achieved by Stark modulation of the MoS₂ material. We demonstrate that this nonlinearity can be fitted and employed as the activation function to facilitate reservoir computing implementation. Notably, owing to the high-order nonlinearity, the network exhibits long-term synchronization and robust generalization abilities for approximating complex dynamical systems. Given the remarkable reservoir activation capability, coupled with the scalability of the device fabrication, our findings open the possibility for the physical realization of lightweight, efficient reservoir computing for, for instance, signal classification, motion tracking, and pattern recognition of complex time series as well as secure cryptography. As an example, we show the network can be appointed to generate chaotic random numbers for secure data encryption.

Introduction

Reservoir computing is a recurrent neural network with a concise three-layer topology, i.e. the input, *reservoir*, and output (1-3). The reservoir is central to the network. By forging the reservoir into a nonlinear dynamical system through long-term iteration, the network can generate complex dynamical patterns through the sparse connectivity of the reservoir for performing regression tasks, such as motion tracking, spatial-temporal pattern recognition, and chaotic attractor reconstruction (4). To ensure long-term iteration, the reservoir requires nonlinear activation at each time step, where the activation functions employed must possess sufficient nonlinearity (5). Otherwise, the reservoir can collapse into linear projections and the network can fail to output reliable predictions on the target (6). Given this, the iteration of the reservoir can result in a heavy computational workload (7). Leon O. Chua back in the 1980s purposed that nonlinear electronic components could cause *non-periodic oscillations*, also known as *chaos phenomena*, in electronic circuits (8). Inspired by this, configuring nonlinear electronic systems as a physical reservoir and harnessing the nonlinearity from the electronic components for activation can be an effective solution to address the computational workload challenge (4, 9). To achieve successful activation of the physical reservoir, the electronic components must possess a sufficient nonlinearity (6, 7).

Semiconductor devices exhibiting nonlinear properties are proven promising in realizing physical reservoir (7, 9). Particularly, devices fabricated from two-dimensional (2D) materials are of a great interest due to their quantum confinement effects and the convenient modulation of their electronic structures (10). Indeed, state-of-the-art advances have demonstrated the feasibility of realizing physical reservoir using 2D material devices (11, 12). Interestingly, the unique (opto)electronic and photonic properties of 2D materials can be coupled for multimodal signal processing (13, 14). Towards physical reservoir realization using 2D material devices, solution-processing holds great promise – it allows for mass production of materials, and the materials are readily adapted to the CMOS processes and printing techniques for large-scale device fabrication and integration (15). Again, to ensure successful activation of the enabled physical reservoir, it is crucial to effectively modulate the electronic structures of solution-processed 2D materials for devices with sufficient nonlinearity. Otherwise, as discussed, the network will be incapable of handling nonlinearly inseparable tasks or chasing complex dynamics. In our recent study (16), we demonstrated that Stark effect could be effective to modulate the electronic structures of solution-processed 2D materials. We showed that the carriers in solution-processed 2D materials could redistribute in local fields due to the Stark effect, and that this Stark modulation could be employed to develop highly nonlinear electronic devices.

In this work, we analyze reservoir activation using the nonlinearity harnessed from solution-processed molybdenum disulfide (MoS_2) devices. We fabricate devices using solution-processed MoS_2 , and harness the nonlinearity from the devices as the activation function for constructing a reservoir computing model. We prove that the nonlinearity quantifies a high-order nonlinearity, and that this nonlinearity ensures reservoir activation in long-term iteration. Notably, the network demonstrates synchronization and generalization for regression of dynamical systems. Meanwhile, as proved in a baseline NARMA-10 test, our reservoir activation approach is robust to the variation of the network parameter settings. The robustness is crucial for the rapid deployment of reservoir computing. To explore the potential application, we show the complex dynamics synchronization ability can be applied in generating chaotic time series for secure cryptography. The results prove the feasibility of employing the nonlinearity from solution-processed MoS_2 devices for reservoir activation, underscoring the potential of realizing lightweight, efficient reservoir computing.

Results

High-order device nonlinearity: We study MoS₂ device fabrication in our work, as MoS₂ is an archetype of 2D materials with robust material properties and, particularly, MoS₂ in mono-, few-layers can allow effective Stark modulation of the electronic structures (16, 17). Figure 1a shows the structure of few-layer MoS₂. As the Stark effect progresses in MoS₂ in the electric field, the carriers in MoS₂ become delocalized and fill in the intra-layer space, forming intra-layer carrier transport layers, as illustrated in Fig. 1b. Applying the Stark modulation to the solution-processed MoS₂, the electrical conductance of the solution-processed nanoflakes and their networks can enhance drastically, leading to nonlinear electrical properties in the enabled devices (16).

We fabricate junction devices from solution-processed MoS₂ following the method reported in our previous study (16). Briefly, MoS₂ produced by liquid-phase exfoliation is deposited along with ferroelectric P(VDF-TrFE) polymer by inkjet printing to fabricate devices in a structure of electrode/MoS₂-P(VDF-TrFE)/electrode (see Supplementary). Figure 1c shows a typical ink of MoS₂. Material characterizations confirm successful exfoliation of MoS₂ and that the as-exfoliated MoS₂ is in the pristine 2H phase (Fig. S1a-d). As shown by the cross-sectional microscopic structure of a typical device (Fig. 1d), the deposited MoS₂ and P(VDF-TrFE) form a composite film where the solution-processed MoS₂ nanoflakes are embedded in the P(VDF-TrFE) after interlayer diffusing during printing. Here the ferroelectric P(VDF-TrFE) can exert local polarization fields to the embedded solution-processed MoS₂ nanoflakes and as such, induce Stark modulation (16). Note that the P(VDF-TrFE) after deposition undergoes ferroelectric crystallization to ensure polarization in external electric fields (Fig. S1e-h).

Upon operation, the devices demonstrate significant nonlinear switching, with a switching ratio of $\sim 10^3$ (Fig. S2a). However, as observed, hysteresis is associated with the switching due to the polarization hysteresis of the ferroelectric P(VDF-TrFE) polymer (16). This can lead to problems with physical reservoir realization – high-frequency data processing by the physical reservoir will require low hysteresis in the devices; otherwise, a prolonged time will be demanded for the devices to forget the previous inputs. To ensure high-frequency data processing for the physical reservoir, the hysteresis must be minimized. Here we purpose a device aging method by cycling the devices with sweeping bias. As charges are injected into and directly pass through the P(VDF-TrFE), the locked dipole states in P(VDF-TrFE) can be easily disrupted, leading to fatigue of the ferroelectric polarization (18). As observed, this fatiguing behavior is demonstrated in the current output of our devices – after a few sweeping cycles, the hysteretic switching quickly degrades to volatile from the initial non-volatile (Fig. S2b); and after a few more sweeping cycles, the hysteresis gradually converges (Fig. S2c), leading to a well-converged nonlinear current output (Fig. 1e).

To quantify the nonlinearity from our well-fatigued devices, we use polynomial regression to describe the well-converged current output,

$$I = \sum_m g_m V^m + \xi, \quad (1)$$

where m is the polynomial order, $\{g_1, g_2, \dots, g_m\}$ is the corresponding coefficient, and ξ is the residual error. Note that polynomial regression is specifically used here for quantifying the degree of nonlinearity as it can suitably and accurately describe the nonlinearity for the following reservoir activation. As proved in Fig. S2e, only when the polynomial reaches a third order or more, the coefficient of determination (R^2) of the fitting is above 0.99 and the mean square error (MSE) is below 0.1. A third order or more quantifies a *high-order nonlinearity* (19). Notably, a 9-th order

polynomial regression can best fit the current output (Fig. 1e). Therefore, our well-fatigued devices prove nonlinear switching with a high-order nonlinearity.

Reservoir activation: Our solution-processed MoS₂ devices hold the potential towards physical reservoir realization, given the high-order nonlinearity and the scalability of the device fabrication. However, a practical realization requires large-scale circuits with high-level integration. This is thus far challenging, especially for lab-scaled demonstrations. Therefore, to illustrate this potential, we perform theoretical study on physical reservoir computing implementation using our solution-processed MoS₂ devices. Figure 2a presents the topology of the echo state network (ESN) studied in our work, where the high-order nonlinearity harnessed from our solution-processed MoS₂ devices is fitted as the activation function, denoted as f_{dev} , and embedded in the reservoir for nonlinearly transforming the input to the reservoir. Note that echo state network is one of the founding models of reservoir computing (20, 21).

The reservoir dynamics of our ESN can be described as,

$$\mathbf{r}_n = f_{\text{dev}}(s_{\text{in}}\widehat{W}_{\text{in}}\mathbf{p}_n + \rho\widehat{W}_{\text{res}}\mathbf{r}_{n-1}), \quad (2)$$

where \widehat{W}_{in} and \widehat{W}_{res} are the weight matrix for the input and the reservoir connections, respectively, with (\mathbf{p}, \mathbf{q}) representing the input-output pair to the ESN. The reservoir is forged into a dynamical system, wherein the present reservoir state \mathbf{r}_n is a function of the past states $\{\mathbf{r}_{n-1}, \mathbf{r}_{n-2}, \dots\}$, with the input scaling s_{in} and reservoir spectral radius ρ being as the hyperparameters of the reservoir. This recurrent topology gives the ESN the potential to approximate and forecast time series signals if proper hyperparameter sets are given (3). Note that, as discussed, the nonlinearity of the activation function is key to maintaining long-term reservoir iteration. Activation function with limited nonlinearity can result in linear superpositions of the past input states and as such, explosion and convergence of the reservoir states. To examine the effectiveness of reservoir activation by the device characteristics, we fit the high-order nonlinear current output from our solution-processed MoS₂ devices and employ it as the activation function, f_{dev} , to nonlinearly transform the inactivated reservoir input, $\mathbf{u}_n = s_{\text{in}}\widehat{W}_{\text{in}}\mathbf{p}_n + \rho\widehat{W}_{\text{res}}\mathbf{r}_{n-1}$. Figure 2b schematically illustrates the nonlinear transformation of the inactivated reservoir input with f_{dev} .

As discussed, the recurrent topology of our ESN determines its suitability to the tasks of time series regression. As dynamical systems are in general time series with hidden patterns, we adopt a weather model proposed by Lorenz in 1963 (22) as the target dynamical system, denoted as *Lorenz-63*, to evaluate the performance of the ESN. By learning the dataset $S = \{P_{\text{train}}, Q_{\text{train}}\} = \{(\tilde{\mathbf{p}}_1^T, \tilde{\mathbf{p}}_2^T, \dots, \tilde{\mathbf{p}}_N^T), (\tilde{\mathbf{q}}_1^T, \tilde{\mathbf{q}}_2^T, \dots, \tilde{\mathbf{q}}_N^T)\}$ extracted from *Lorenz-63*, the output connection weight \widehat{W}_{out} can be optimized by the Tikhonov regularization (23),

$$\widehat{W}_{\text{out}} = Q_{\text{train}}R_{\text{train}}^T(R_{\text{train}}R_{\text{train}}^T + \alpha^2\hat{\mathbf{I}})^{-1}, \quad (3)$$

where $R_{\text{train}} = (\mathbf{r}_1^T, \mathbf{r}_2^T, \dots, \mathbf{r}_N^T)$ is the reservoir state matrix generated by the reservoir during the training phase, $\hat{\mathbf{I}}$ is the identity matrix with a dimension of $N \times N$, and α is the regularization factor. Note that during the training phase, the reservoir is left untrained, and only the output connection weight \widehat{W}_{out} is optimized. As demonstrated by the training results in Fig. 2c and e, the ESN successfully learns the hidden dynamics of *Lorenz-63*. For example, during the training phase, corresponding to time step 0 to 3,000, the absolute deviation between the target ground truth and the ESN prediction at each time step n , $\text{error}(n) = \|\tilde{\mathbf{q}}_n - \mathbf{q}_n\|_2$, remains nearly zero, proving a successful replication of *Lorenz-63* by the ESN. This demonstrates that our ESN has learned the dynamics of *Lorenz-63* successfully and sufficiently.

In the forecasting phase, using the output connection weight for projecting the high-dimensional reservoir states back to the real space where *Lorenz-63* locates, $\mathbf{q}_n = \widehat{W}_{\text{out}} \mathbf{r}_n$, we aim to predict the evolutionary trends of *Lorenz-63*. As demonstrated by the forecasting results in Fig. 2d and e, the ESN successfully predicates the dynamics of *Lorenz-63*. Following the above training phase, i.e. beyond time step 3,000, the ESN enters the forecasting phase to predict the evolutionary trends of *Lorenz-63*. As observed, in the short term from time step 3,000 to 3,700, the ESN precisely predicts the *Lorenz-63* evolution. However, as it goes beyond time step 3,700, the ESN starts to drift from the ground truth, and the absolute deviation starts to rise. Nevertheless, the precise short-term prediction of the ESN, in addition to the successful replication of *Lorenz-63*, proves successful activation of the reservoir by using the activation function, f_{dev} , fitted from the high-order nonlinearity from the solution-processed MoS₂ devices.

Dynamical system synchronization: Bounded activation functions such as *tanh* and *sigmoid* are often adopted in reservoir computing to ensure asymptotically convergence and continuity of the reservoir states during long-term recurrence, known as the *echo state property* (6, 24, 25). Otherwise, the reservoir states can explode or converge rapidly (6, 20). To guarantee the *echo state property*, the reservoir dynamics must satisfy the *Lipschitz continuity* (6, 26). In our case, as the fitted activation function, f_{dev} , acts element-wisely on the reservoir inputs, we consider the basic one-dimensional input-output circumstance. Therefore, for two arbitrary reservoir states r_n and r'_n , we have

$$\begin{aligned} \|r_n - r'_n\|_2 &= \|f_{\text{dev}}(s_{\text{in}} w_{\text{in}} p_n + \rho w_{\text{res}} r_{n-1}) - f_{\text{dev}}(s_{\text{in}} w_{\text{in}} p_n + \rho w_{\text{res}} r'_{n-1})\|_2 \\ &= \left\| \sum_m g_m [(s_{\text{in}} w_{\text{in}} p_n + \rho w_{\text{res}} r_{n-1})^m - (s_{\text{in}} w_{\text{in}} p_n + \rho w_{\text{res}} r'_{n-1})^m] \right\|_2. \end{aligned} \quad (4)$$

However, the polynomial current-output demonstrated from our solution-processed MoS₂ devices seems to violate the bounded condition required for the Lipschitz continuity, as the unbounded current output can increase to infinity (Fig. 1e). Fortunately, the operational range can be readily confined by adjusting the input scaling s_{in} , as the input to the reservoir is a function of input scaling where $u_n = U(s_{\text{in}}) = s_{\text{in}} w_{\text{in}} p_n + \rho w_{\text{res}} r_{n-1}$. Besides guaranteeing the Lipschitz continuity, it is of benefits to the practical operation of the devices – as the input signals are encoded into voltage signals, high voltage signals can lead to current overflows and damage the devices. By setting a proper operational range, the current output from the devices can be effectively confined. As the fitted activation function, f_{dev} , is monotonic, the reservoir states can satisfy the Lipschitz continuity in the operational range $u_n \in [V_{\text{min}}, V_{\text{max}}]$ by

$$\|r_n - r'_n\|_2 \leq \left\| \sum_m g_m [(V_{\text{max}})^m - (V_{\text{min}})^m] \right\|_2 = \|f_{\text{dev}}(V_{\text{max}}) - f_{\text{dev}}(V_{\text{min}})\|_2, \quad (5)$$

ensuring the echo state property during long-term recurrence.

As demonstration, we limit the operational range of the devices to -4V to 4V where the nonlinear current output can be well-bounded, and examine the long-term synchronization ability of our ESN to *Lorenz-63* using the fitted activation function, f_{dev} . Specifically, in the long-term synchronization test, the time step length of the training phase is set to be 1,000 (instead of 3,000) for short-term initiation of the ESN, while the forecasting phase is 10,000 (instead of 3,000). As demonstrated in Fig. 3a-c, by learning the dynamics of *Lorenz-63* for a short-term, the ESN can perfectly reconstruct the long-term climate, the Lorenz attractor, of *Lorenz-63*.

The difference in the chaos behavior between Lorenz-63 and the ESN reconstruction may give insights to the effectiveness of the fitted activation function, f_{dev} , for activating the reservoir. Given an arbitrary discrete dynamical system $\psi_{n+1} = \Phi(\psi_n)$ with an initial state (ψ_0), the *maximal Lyapunov exponent* (MLE),

$$\lambda(\psi_0) = \lim_{n \rightarrow \infty} \frac{1}{n} \sum_{i=0}^{n-1} \ln|\Phi'(\psi_i)|, \quad (6)$$

can be considered as an indicator characterizing the dynamical behavior of the system (27). Following the method proposed by M. T. Rosenstein et al. (28), we estimate the MLE of Lorenz-63 and the ESN reconstruction. As demonstrated in Fig. 3d, both the ESN reconstruction (i.e. the network output) and the *Lorenz-63* attractor (i.e. the target ground truth) exhibit positive MLE, proving chaotic behaviors. In addition, the similarity in MLE (1.168 vs. 1.166) indicates successful approximation of the chaotic characteristics of the Lorenz-63 attractor. This demonstrates the *generalized synchronization property* (29) of our ESN, meaning that the network perfectly replicates the chaotic attractor. More importantly, as presented in Fig. 3e, the ESN maintains within the operational range of -4V to 4V set for the devices, proving the effectiveness of the fitted activation function, f_{dev} , for long-term recurrence in operation.

Generalization with robustness: The generalization ability is crucial for an ESN to adapt to the diverse data sets and handle the different application scenarios. For model-free machine learning approaches, including ESN, capturing the differences in the evolutionary trends of the target systems based on the given dataset is the cornerstone ability of generalization. Back to the dynamical system regression scenario, the different system parameters can lead to varying evolutionary trends. Whether our ESN is capable of capturing the evolutionary trends reflects its generalization ability and also the effectiveness of our approach of using device nonlinearity for reservoir activation. Here, we adopt a single parameter controlled 2D logistic map,

$$\begin{cases} x_{n+1} = h(3y_n + 1) \cdot x_n \cdot (1 - x_n) \\ y_{n+1} = h(3x_{n+1} + 1) \cdot y_n \cdot (1 - y_n) \end{cases}, \quad (7)$$

as the target system to closely examine the generalization ability of our ESN. In general, as shown in Fig. 4a, as the control parameter h increases, the system evolutionary behavior transits from convergence to periodic oscillation and, ultimately, chaotic behavior. For example, as shown by the system evolutionary phase portrait in Fig. 4b, when h is 1.13, the stabilized target exhibits periodic oscillations, and the ESN easily learns this behavior. When h increases to 1.16, the target is near the bifurcation point, also known as *edge-of-chaos*, and begins to oscillate back and forth between several steady states; the ESN effectively learns the jumping state of the target. Note that due to the synchronization ability of the ESN, instead of perfectly replicating the target, the ESN predicts a higher number of steady states, including the ground truth ones. Eventually, when h reaches 1.19, the target enters chaos, and the ESN perfectly predicts the chaotic oscillation of the target. As shown in Fig. S3 and 4, we then investigate the learning ability of the ESN for dynamical systems of varying dimensions from 1D to 3D. As summarized in Table. SI, the results prove the outstanding performance of the ESN in chaotic pattern replication for the dynamical systems with varying dimensions. In all cases, the ESN successfully reconstructs the chaotic time series and presents similar MLE. This proves that using the activation function, f_{dev} , fitted from the high-order nonlinearity from our solution-processed MoS₂ devices enables the generalization ability.

As discussed, the reservoir itself is a dynamical system where varying the hyperparameter sets can lead to impacts to the evolutionary trends of the reservoir. Although proper output connection

weight optimized by Tikhonov regularization can help project rich and diverse reservoir dynamics to the target systems, there are still boundaries. The abundance of effective hyperparameter sets, or alternatively, the robustness of the activation functions to the hyperparameter sets, determines the difficulty in setting up a functionable ESN model for applications. Specifically, an overly stringent hyperparameter feasible region means that the network requires more refined and complicated optimization methods; on the contrary, a wider range of hyperparameter choices means a stronger stability of the network. To examine the robustness of the fitted activation function, f_{dev} , to the hyperparameters, we appoint the ESN to learn the NARMA-10 task. Note that NARMA-10 is a commonly used benchmark for testing the performance of recurrent neural networks (30). The NARMA-10 task series can be generated by (31):

$$\tilde{y}_{n+1} = 0.3\tilde{y}_n + 0.05\tilde{y}_n \left[\sum_{i=0}^9 \tilde{y}_{n-i} \right] + 1.5v_n v_{n-1} + 0.1, \quad (8)$$

where the input v is a random scalar input drawn from the uniform distribution in the interval $[0, 0.5]$. As demonstrated in Fig. 4c, the ESN perfectly handles the NARMA-10 task by replicating the complex dynamics of the ground truth. Note that as shown in Fig. 4d when the input scaling s_{in} is higher than 3.2, the coefficient of determination R^2 between the ground truth and the ESN prediction, $R^2 = 1 - \sum_i (q_i - \tilde{q}_i) / \sum_i (\tilde{q}_i - \langle \tilde{q} \rangle)$, reaches 0.8 and higher. This aligns with our discussion on the input scaling and operational range – a higher input scaling means a wider operational range and leads to larger oscillations in the reservoir states. As such, the larger input scaling makes the ESN run at the edge-of-chaos with a better ability to approximate rich and diverse complex dynamics, in other words, showing generalization ability.

Our ESN running at the edge-of-chaos, however, may not be robust as the fitted activation function, f_{dev} , may not be well bounded and the reservoir may as such lack negative feedback as a result. To investigate this, we carry out a cross-validation examination to forecast NARMA-10 by 20 iterations using $s_{\text{in}} = 4 > 3.2$. As shown in Fig. 4e, the ESN presents robust performance, giving an averaged coefficient of determination R^2 over 0.9. Further, we variate the other hyperparameters to test whether the robust ESN performance can be maintained. As demonstrated in Fig. 4f, as long as the reservoir spectral radius ρ exceeds 0.5, the ESN guarantees long-term recurrence at the *edge-of-chaos*, and generates reliable outcomes, general for the reservoir with a wide range of sparsity (reservoir density ranging from 0.1 to 0.5). The results prove that the activation function, f_{dev} , fitted from the high-order nonlinearity from our solution-processed MoS₂ devices is robust to a wide range of hyperparameter sets, critical for the implementation and the rapid deployment of practical physical reservoir computing hardware.

Application in secure cryptography: Our ESN has been proven to be effective and robust in long-term synchronizing of various dynamical systems. This can be exploited to generate chaotic series by appointing the ESN to learn and imitate a teacher system. The hidden dynamics of the teacher system generated by mathematical algorithms are reproducible, while the chaotic series output by ESN expects to exhibit similar yet differentiated dynamical characteristics to the hidden dynamics. This determines the chaotic series difficult to be reproduced or deciphered, promising for applications in secure cryptography. Figure 5a illustrates an asymmetric encryption strategy, where the ESN acts as a chaotic random number generator, and the hyperparameter sets of the ESN are used as the authentication information to be transmitted by the service provider to the end-users. Particularly, to ensure the security, the authentication information alone cannot complete the verification. Only when both the authentication information and device

characteristics are available, a proper authentication key can be generated. In this context, to design a secure cryptographic system, the solution-processed MoS₂ devices can be used to serve as hardware key generators for distribution to the end-users.

To investigate the feasibility of using our ESN in secure cryptography, we test its ability to generate chaotic random numbers. Here, we use a 2D chaotic system as the teacher system,

$$\begin{cases} x_{n+1} = \sin\{\pi[4hx_n(1-x_n)] + (1-h) \cdot \sin(\pi y_n)\} \\ y_{n+1} = \sin\{\pi[4hy_n(1-y_n)] + (1-h) \cdot \sin(\pi x_{n+1}^2)\} \end{cases}, \quad (9)$$

and then appoint the ESN to learn its hidden dynamics for the generation of differentiated chaotic random numbers. As shown in Fig. 5b, the learned ESN generates a set of uniformly yet randomly distributed points within the interval, $\{(x, y) | 0 \leq x \leq 1, 0 \leq y \leq 1\}$. See also Fig.S5 for the comparison between the teacher system and the ESN reconstruction. By converting these points into $x - y$ bit pairs, a series of 00, 01, 10, and 11 bit pairs can be generated. Statistical study conducted on 2,500 bit pairs show that the occurrence frequency for each of the bit pairs is $\sim 25\%$ (Fig. 5b), proving a good uniformity. To verify the randomness of the bit stream generated by the ESN, we conduct a standard statistical test of the ESN output using the NIST Special Publication 800-22 test suite (32). As demonstrated in Fig. 5c, the chaotic random numbers pass 13 out of 15 NIST tests, suggesting a randomness potentially sufficient for secure cryptographic applications.

We perform symmetric-key image encryption using the random bit streams generated by the ESN. The Advanced Encryption Standard (AES) algorithm is used here for encryption and decryption. Figures 5d shows successful symmetric-key image encryption in an AES-CBC mode, and as observed the image information is well masked and perfectly restored. More explicitly, the uniform color statistical distributions in the color channels of red, green, and blue show that the encrypted image has a uniform distribution throughout the pixel value range from 0 to 255. Meanwhile, the proportion of these three color channels are at the same level, suggesting that the information is well hidden. The color distributions before and after encryption is also consistent, proving that the chaotic random numbers generated by the ESN can indeed be used to enable secure cryptography. See also Fig. S5 for the symmetric-key image encryption in the AES-ECB mode. The results provide a theoretical foundation of using our ESN in secure cryptography.

Conclusion

In this work, we have analyzed and validated the feasibility of employing the nonlinearity from solution-processed MoS₂ devices for reservoir activation. The devices demonstrate a high-order nonlinearity, achieved through Stark modulation of the solution-processed MoS₂. We show that the nonlinearity can be fitted as the activation function and embedded in the reservoir to implement echo state network. Particularly, owing to the high-order nonlinearity, the network proves long-term synchronization, and is general and robust to various hyperparameter sets. Generalization with robustness is critical for the rapid deployment of reservoir computing, while generalized long-term synchronization to dynamical systems is promising to enable complex dynamics chasing and chaotic attractor reconstruction in various applications, for example, secure cryptography. As an example, we appoint the network to generate chaotic random numbers for data encryption. The remarkable reservoir activation capability, coupled with the scalability of the device fabrication, suggests the potential for realizing lightweight, efficient physical reservoir computing that may extend the modern embedded systems for high-efficiency data processing and computing in, for instance, unveiling signal patterns of IoT sensors and healthcare systems, and tracking motions in wearables and soft robotics beyond secure cryptography.

References

- [1] Jaurigue, L. and Ludge, K. Connecting reservoir computing with statistical forecasting and deep neural networks. *Nat. Commun.* **13**, 227 (2022).
- [2] Schrauwen, B., Verstraeten, D. and Van Campenhout, J. An overview of reservoir computing: theory, applications and implementations. In *Proceedings of the 15th european symposium on artificial neural networks (ESANN)* 471-482 (2007).
- [3] Lukosevicius, M. and Jaeger, H. Reservoir computing approaches to recurrent neural network training. *Comput. Sci. Rev.* **3**, 127-149 (2009).
- [4] Yan, M., et al. Emerging opportunities and challenges for the future of reservoir computing. *Nat. Commun.* **15**, 2056 (2024).
- [5] Gonon, L., Grigoryeva, L. and Ortega, J. P. Memory and forecasting capacities of nonlinear recurrent networks. *Physica D* **414**, 132721 (2020).
- [6] Jaeger, H., et al. Optimization and applications of echo state networks with leaky-integrator neurons. *Neural Netw.* **20**, 335-352 (2007).
- [7] Tanaka, G., et al. Recent advances in physical reservoir computing: A review. *Neural Netw.* **115**, 100-123 (2019).
- [8] Matsumoto, T., Chua, L. O. and Komuro, M. The Double Scroll. *IEEE Trans. Circuits Syst.* **32**, 797-818 (1985).
- [9] Liang, X. P., et al. Physical reservoir computing with emerging electronics. *Nat. Electron.* (2024).
- [10] Novoselov, K. S., et al. 2D materials and van der Waals heterostructures. *Science* **353**, 6298 (2016).
- [11] Wei, Z. Reservoir computing with 2D materials. *Nat. Electron.* **5**, 715-716 (2022).
- [12] Sun, L., et al. In-sensor reservoir computing for language learning via two-dimensional memristors. *Sci. Adv.* **7**, eabg1455 (2021).
- [13] Liu, C., et al. Two-dimensional materials for next-generation computing technologies. *Nat. Nanotech.* **15**, 545-557 (2020).
- [14] Du, L., et al. Engineering symmetry breaking in 2D layered materials. *Nat. Rev. Phys.* **3**, 193-206 (2021).
- [15] Conti, S., et al. Printed transistors made of 2D material-based inks. *Nat. Rev. Mater.* **8**, 651-667 (2023).
- [16] Liu, S., et al. Conduction Modulation of Solution-Processed 2D Materials. *Adv. Electron. Mater.* (2024).
- [17] Ramasubramaniam, A., Naveh, D. and Towe, E. Tunable band gaps in bilayer transition-metal dichalcogenides. *Phys. Rev. B* **84**, 205325 (2011).
- [18] Lou, X. J., et al. Local phase decomposition as a cause of polarization fatigue in ferroelectric thin films. *Phys. Rev. Lett.* **97**, 177601 (2006).
- [19] Burden, R. L. and Faires, D. J., *Numerical Analysis*. (Cengage Learning, 2012).
- [20] Jaeger, H. The “echo state” approach to analysing and training recurrent neural networks. *GMD Report 148*, German National Research Center for Information Technology (2001).
- [21] Jaeger, H. and Haas, H. Harnessing Nonlinearity: Predicting Chaotic Systems and Saving Energy in Wireless Communication. *Science* **304**, 78-80 (2004).
- [22] Lorenz, E. N. Deterministic Nonperiodic Flow. *J. Atmos. Sci.* **20**, 130-141 (1963).
- [23] Hook, A. G. H. J. L. and Dawes, J. H. P. Echo State Networks trained by Tikhonov least squares are $L_2(\mu)$ approximators of ergodic dynamical systems. *Physica D* **421**, 132882 (2021).

- [24] Buehner, M. and Young, P. A tighter bound for the echo state property. *IEEE Trans. Neural. Netw.* **17**, 820-824 (2006).
- [25] Yildiz, I. B., Jaeger, H. and Kiebel, S. J. Re-visiting the echo state property. *Neural Netw.* **35**, 1-9 (2012).
- [26] Dong, J., et al. Asymptotic stability in reservoir computing. In *2022 International Joint Conference on Neural Networks (IJCNN)* (2022).
- [27] Gilpin, W. Generative learning for nonlinear dynamics. *Nat. Rev. Phys.* **6**, 194–206 (2024).
- [28] Rosenstein, M. T., Collins, J. J. and De Luca, C. J. A practical method for calculating largest Lyapunov exponents from small data sets. *Physica D* **65**, 117-134 (1993).
- [29] Lu, Z., Hunt, B. R. and Ott, E. Attractor reconstruction by machine learning. *Chaos* **28**, 061104 (2018).
- [30] Appeltant, L., et al. Information processing using a single dynamical node as complex system. *Nat. Commun.* **2**, 468 (2011).
- [31] Atiya, A. F. and Parlos, A. G. New results on recurrent network training: unifying the algorithms and accelerating convergence. *IEEE Trans. Neural. Netw.* **11**, 697-709 (2000).
- [32] Barker, E. B. and Kelsey, J. M. Recommendation for Random Number Generation Using Deterministic Random Bit Generators. *Special Publication (NIST SP)*, National Institute of Standards and Technology (2015).

Acknowledgements

Funding: GHH acknowledges support from CUHK (4055115) and NSFC (62304196), YYW and JFP from RGC (24200521), Yang Liu from SHIAE (RNE-p3-21), TM from PolyU (P0042991), Yue Lin from NSFC (52273029), Fujian Science & Technology Innovation Laboratory for Optoelectronic Information of China (2021ZZ119), Pilot Project of Fujian Province (2022H0037), Fuzhou Technology Innovation Platform (2022-P-020), Natural Science Foundation of Fujian Province for Distinguished Young Scholars (2023J06045), and Fujian-CAS joint STS Project (2023T3064), and GW from NSFC (12074033), BIT Science and Technology Innovation plan (2022CX01007).

Author contributions: SWL, GHH designed the experiments. SWL, YL, YYW, JFP, XYF, PYL, LKS, WCY, DMP performed the experiments. SWL, GHH analyzed the data. SWL, GHH prepared the figures. SWL, GHH wrote the manuscript. All authors discussed the results from the experiments and commented on the manuscript.

Competing interests: The authors declare no competing financial interests.

Data and materials availability: The data that support the findings of this study are available from the corresponding authors upon request.

Figures

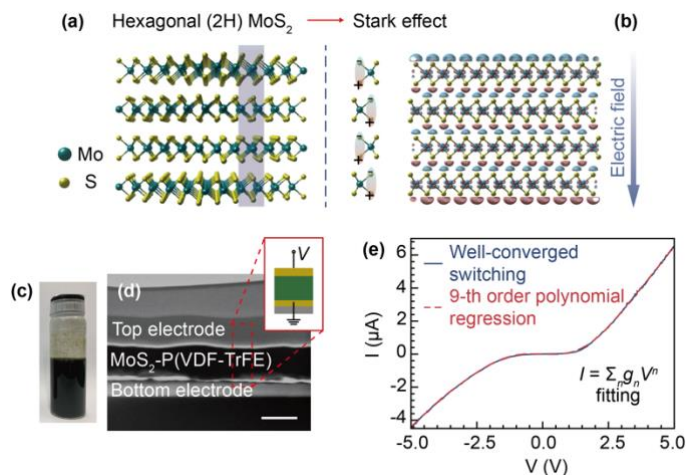


Figure 1. Solution-processed nonlinear MoS₂ junction devices. (a) Schematic structure of few-layer MoS₂, and (b) the formation of conductive two-dimensional carrier transport layers due to the Stark effect. (c) Photo of an as-formulated MoS₂ ink. (d) Cross-sectional microscopic image of a typical device, and the schematic device structure. (e) Well-converged nonlinear current output from the device, demonstrating 9-th order polynomial regression fitting.

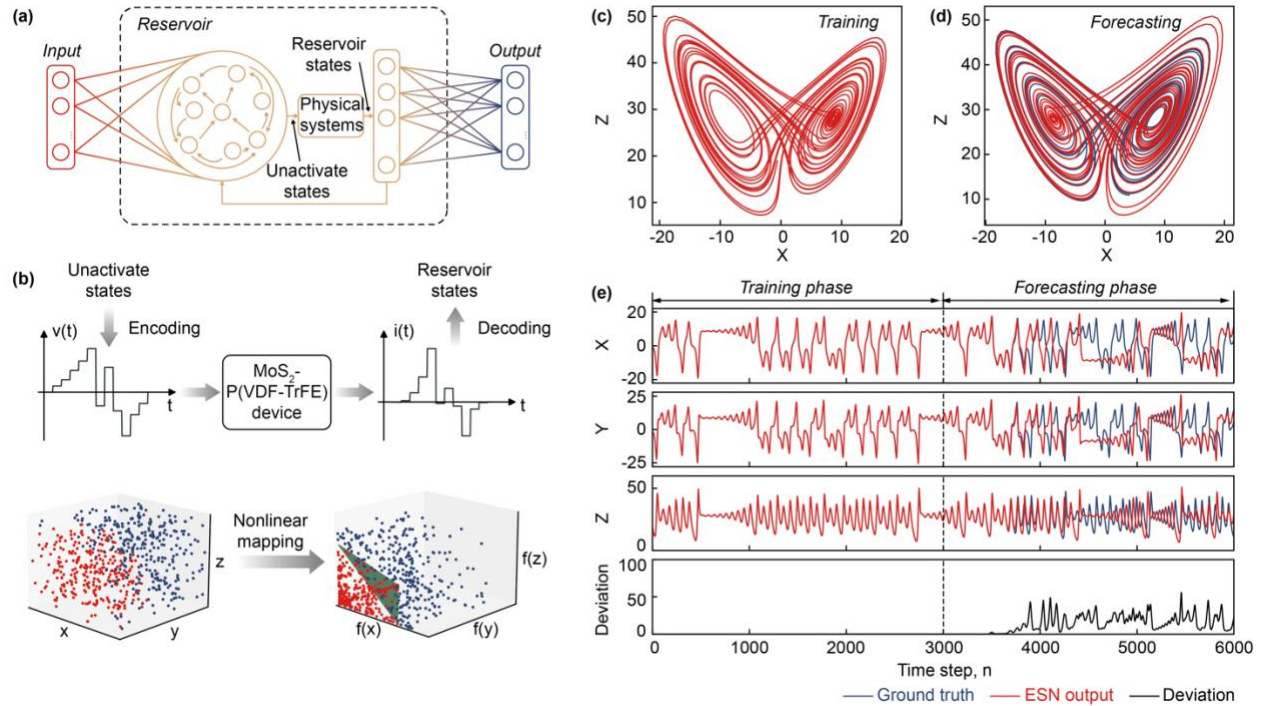


Figure 2. Reservoir activation. (a) Topology of the echo state network (ESN), where the reservoir employs the activation function fitted by harnessing high-order nonlinearity from the solution-processed MoS_2 devices. (b) Schematic reservoir state activation, where the states are nonlinearly mapped by the fitted activation function for activation. Performance of the network in *Lorenz-63* approximation task: (c, d) X-Z portraits during the training and forecasting phases; (e) X, Y and Z time series plots, and the corresponding real-time absolute deviation of the network output from the ground truth.

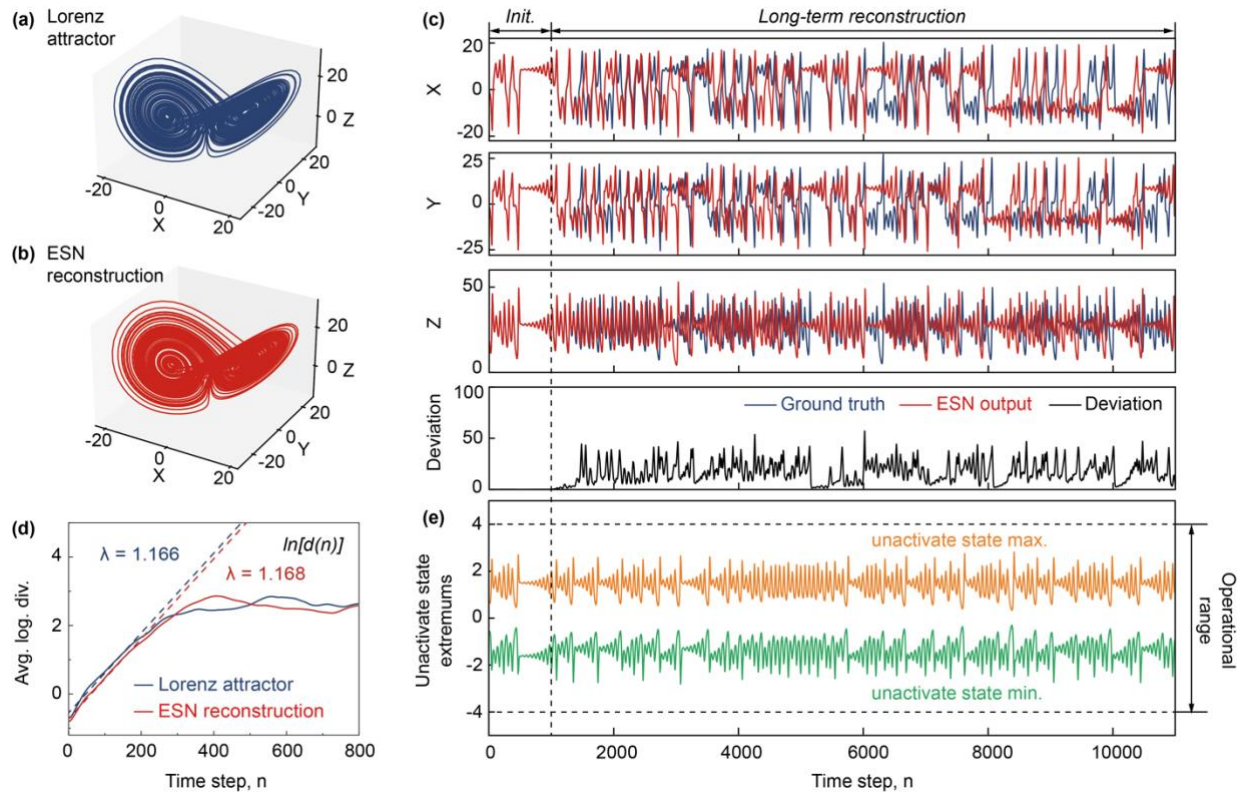


Figure 3. Long-term synchronization of the ESN. 3D visualization of (a) the target *Lorenz-63* system, and (b) the ESN reconstruction in long-term recurrence. (c) X, Y and Z time series plots in long-term ESN reconstruction, and the corresponding real-time absolute deviation of the network reconstruction from the ground truth. (d) *Lyapunov* exponent analysis of the target *Lorenz-63* system and the ESN approximation, showing a *generalized synchronization property* of the ESN. The solid and dashed lines are the experimental and fitted curves, respectively. (e) Real-time input unactivated states to the reservoir, showing strict confinement to the operational range from -4 V to 4 V during the long-term recurrence.

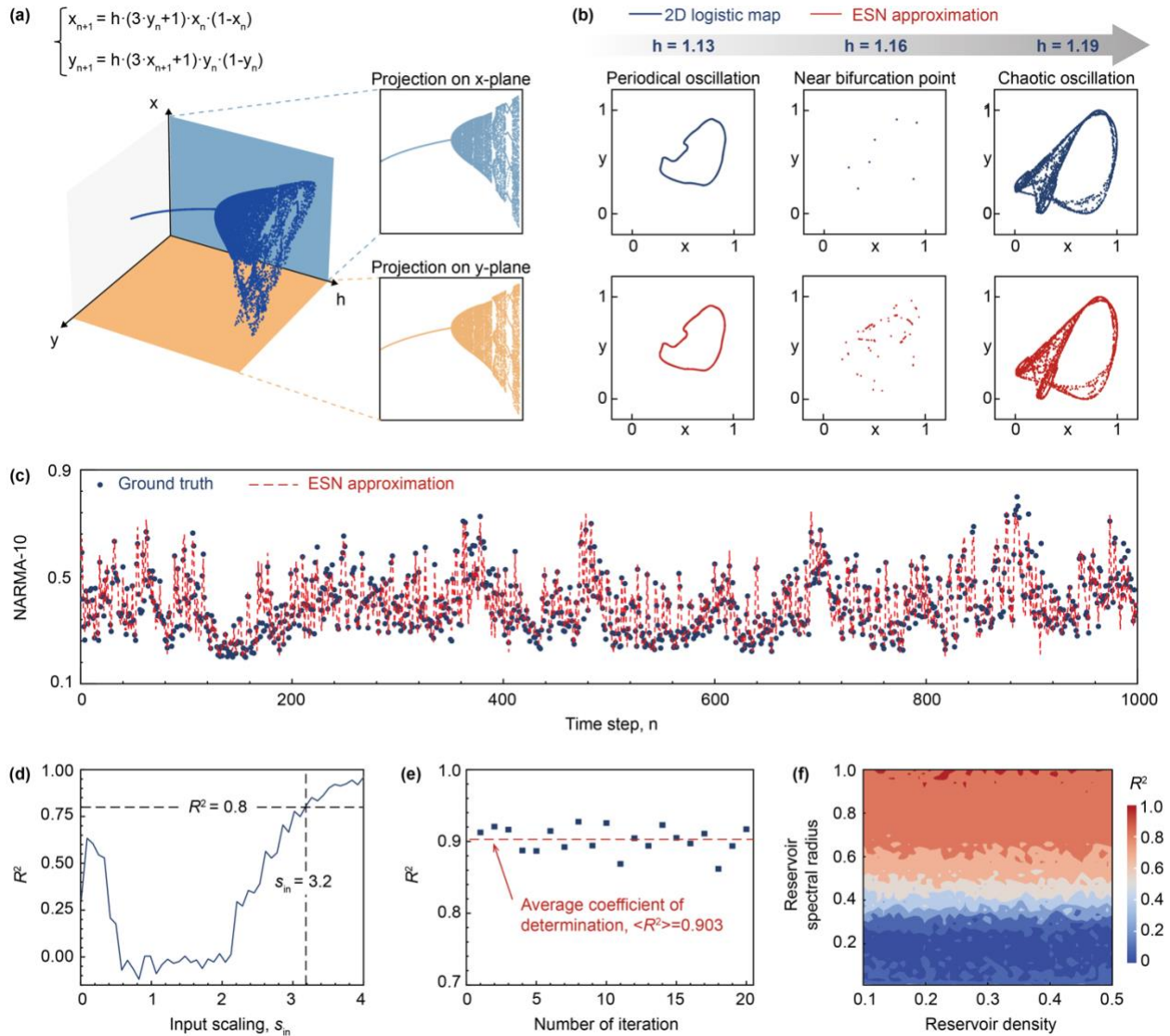


Figure 4. Generalization ability with robustness to varying hyperparameters. (a) The bifurcation map of a single parameter controlled 2D dynamical system. (b) The dynamical system forecasting result of the ESN to the system with the different behaviors. The phase portraits shown at $h = 1.13, 1.16$ and 1.19 prove the generalization ability of the ESN. (c) Typical approximation results for the task NARMA-10 by the ESN, showing great agreement between the ESN approximation and the ground truth. (d) The dependency of the network coefficient of determination R^2 on the input scaling s_{in} , showing the ESN gives credible approximation when the input scaling is over 3.2. (e) The cross-validation of the ESN performance, showing that the ESN achieves an averaged coefficient of determination R^2 of over 0.9 at optimized hyperparameters. The results prove robustness of the generalization performance of the ESN. (f) The NARMA-10 performance of the ESN with the different reservoir density and spectral radius. The ESN exhibits good performance ($R^2 \sim 1$) to a wide range of reservoir density and spectral radius combination, showing fitted action function is robust to the hyperparameter variation.

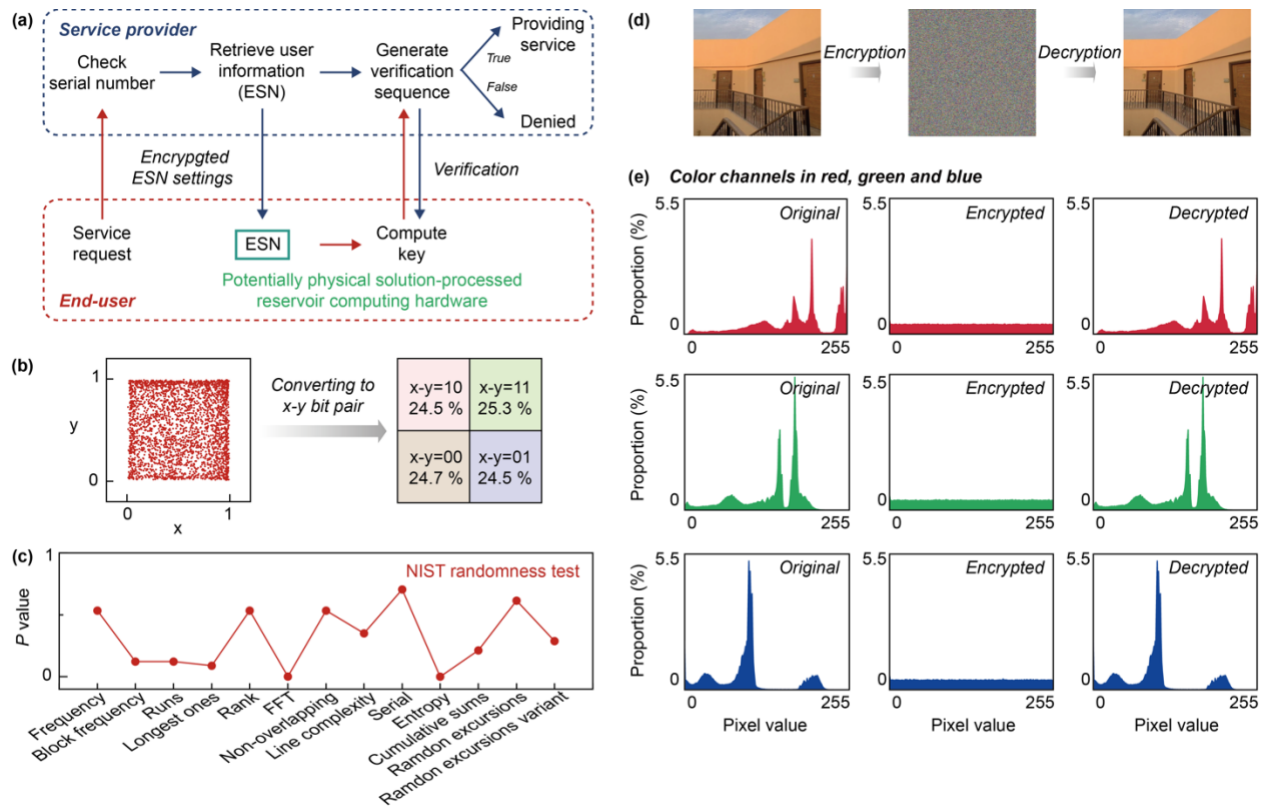


Figure 5. Application in secure cryptography. (a) Schematic diagram of authentication scenario between the service provider and the end-user, where the ESN is used as the chaotic random number generator to generate the authentication keys. (b) Schematic illustration of the random bit stream generation via synchronization a chaotic system using the ESN. The left subplot is the phase portrait of the ESN reconstruction result, while the right subplot is the statistical study of the random bit pairs generated by the ESN. The proportion of the 00, 01, 10, and 11 bit pairs are all around 25 %, proving a good uniformity. (c) NIST test result of the chaotic random numbers generated by the ESN, proving the randomness of the chaotic random numbers. (d) Encryption and decryption of an image and (e) the corresponding color distributions using the chaotic random numbers generated by the ESN. The chaotic random number generated by the ESN can effectively mask the information, and the masked information can be perfectly recovered, proving the effectiveness of the ESN random number generator in the application of secure cryptography.

Supplementary Note

Solution-processed MoS₂ device fabrication: The devices are fabricated following our previous report (1). Briefly, MoS₂ is liquid-phase exfoliated in N-Methyl-2-pyrrolidone (NMP) and then solvent-exchanged into isopropanol/2-butanol (90/10 vol.%) to prepare a 0.5 wt.% inkjet-printable ink. Ferroelectric P(VDF-TrFE) (70:30) polymer is dissolved in N,N-dimethylformamide (DMF) to form a 2.5 wt.% inkjet-printable ink. The MoS₂ and P(VDF-TrFE) inks are then deposited via inkjet printing by Fujifilm Dimatix Materials Printer DMP-2831 to fabricate the vertical junction devices where MoS₂ and P(VDF-TrFE) are sandwiched between the electrodes. The ink cartridge is Dimatix DMC-11610, with a jetting nozzle diameter of 22 μm. The electrodes (e.g. gold and/or ITO) are deposited by evaporation and patterned by shadow-mask. DMF is purchased from Alfa Aesar, and the other materials are from Sigma-Aldrich. All materials are used as received.

Device characterizations: The current output of the junction devices is measured by Keithley 4200A-SCS. The polarisation mapping is measured by atomic force microscope (Bruker Dimension Icon) with a resonant-enhanced piezoresponse force microscopy mode.

Supplementary Figures

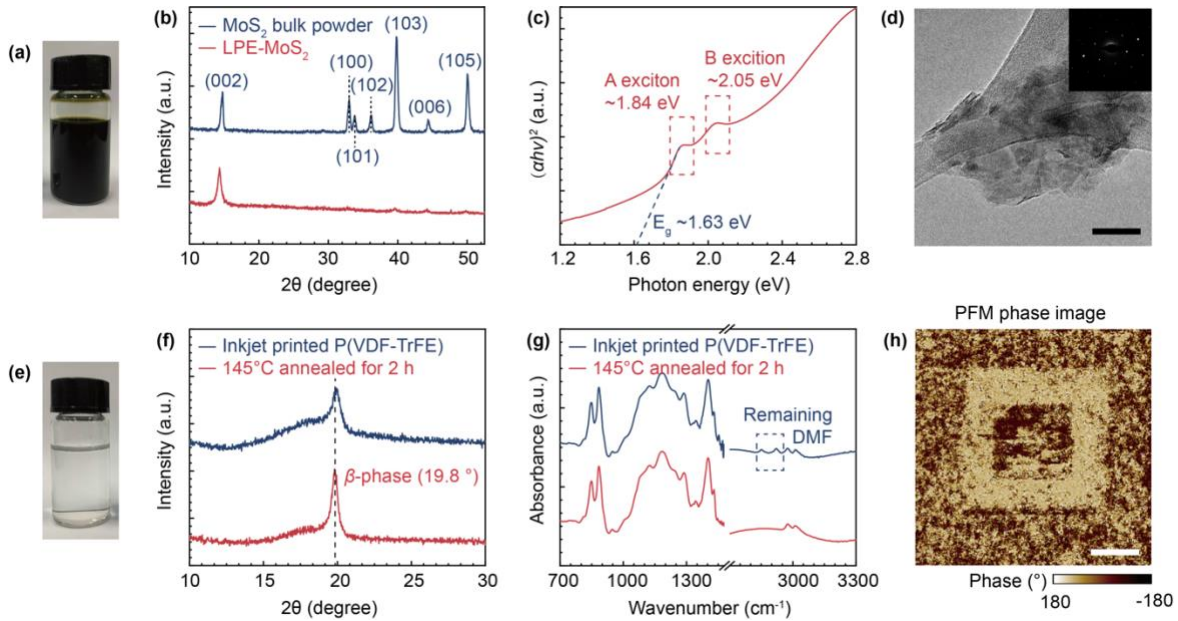


Figure S1. Characterizations of MoS₂ and P(VDF-TrFE). (a) Photo of the dispersion of as-exfoliated MoS₂ in NMP. (b) X-Ray diffraction (XRD) spectral of the raw bulk and as-exfoliated MoS₂, showing successful exfoliation of MoS₂ and proving that the as-exfoliated MoS₂ is in the intrinsic hexagonal (2H) phase. (c) Optical absorption spectrum of the dispersion of as-exfoliated MoS₂, indicating an averaged bandgap of ~1.63 eV for the as-exfoliated MoS₂. (d) Transmission electron microscopic (TEM) image of the as-exfoliated MoS₂ nanoflakes. (e) Photo of a dispersion of P(VDF-TrFE) in DMF. (f) XRD spectral of the as-printed P(VDF-TrFE) thin-film and that after annealing, proving ferroelectric crystallization of the P(VDF-TrFE) by annealing. (g) Fourier-transform infrared spectral of the as-printed P(VDF-TrFE) thin-film and that after annealing, showing the as-printed thin-film is dried with no residual DMF after annealing. (h) Piezo-response force microscopic (PFM) mapping of the ferroelectric crystallized P(VDF-TrFE) thin-film, proving successful ferroelectric polarization. Scale bars – (d) 50 nm, and (h) 1 μm.

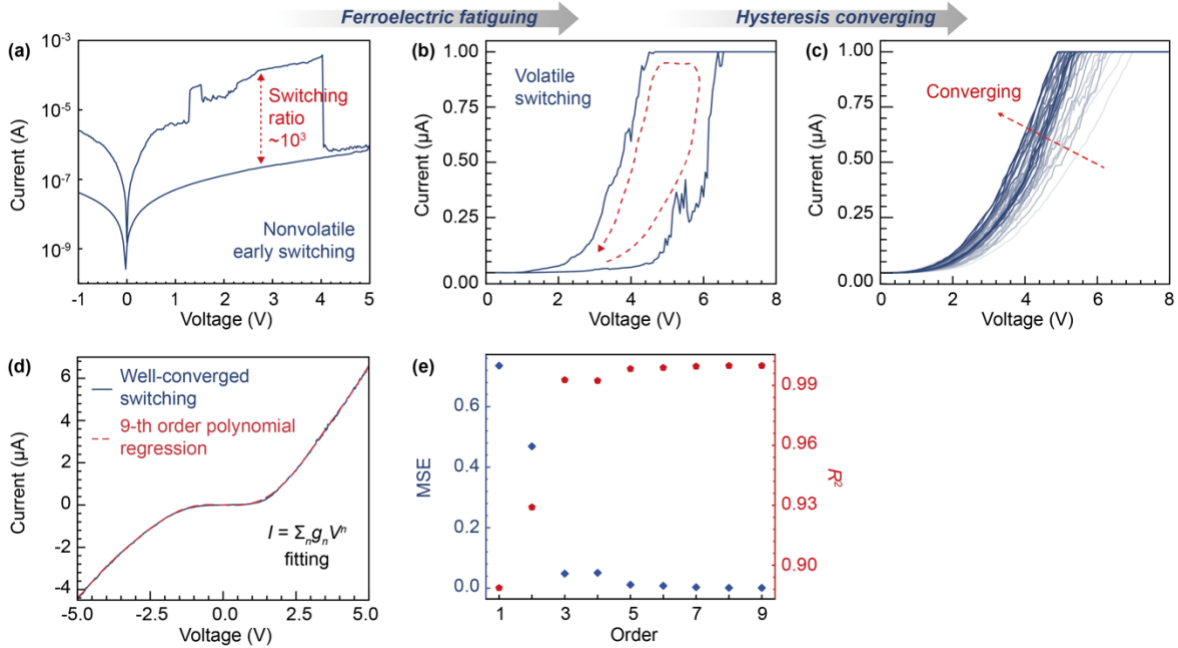


Figure S2. Nonlinear current output from the solution-processed MoS₂ devices. (a) Initial nonlinear current output with significant hysteresis from a typical device, with a high/low resistive state switching ratio of ~10³. (b) Hysteresis fading to volatile switching, and (c) the converging in the switching by fatiguing the P(VDF-TrFE) via bias sweeping. (d) Well-converged nonlinear current output, and the polynomial regression fitting of the current output, replotted from Fig. 1e. (e) The mean square error (MSE) and coefficient of determination (R²) for the polynomial regression fitting at the different fitting orders.

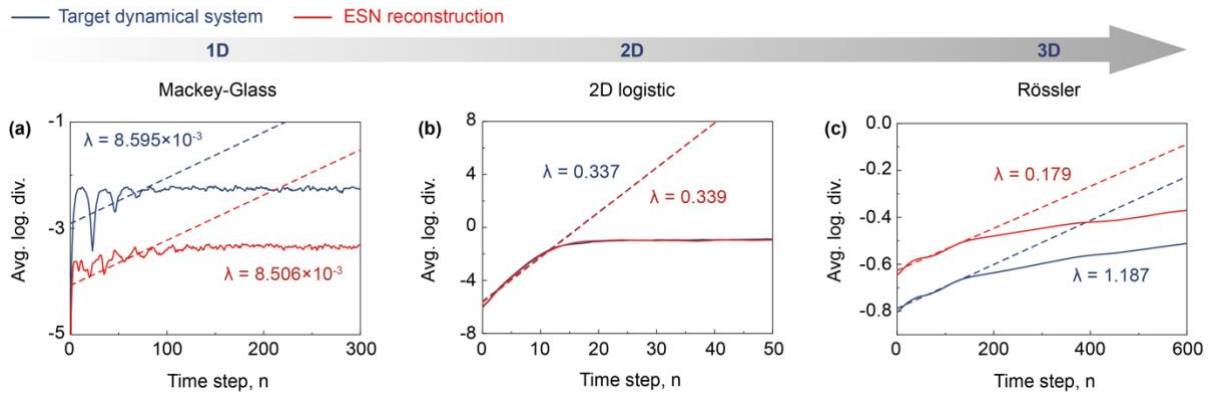
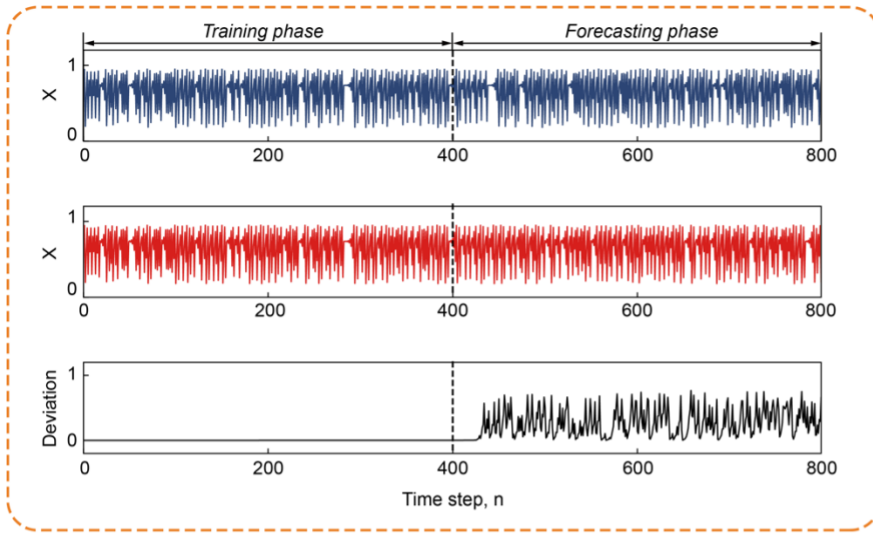
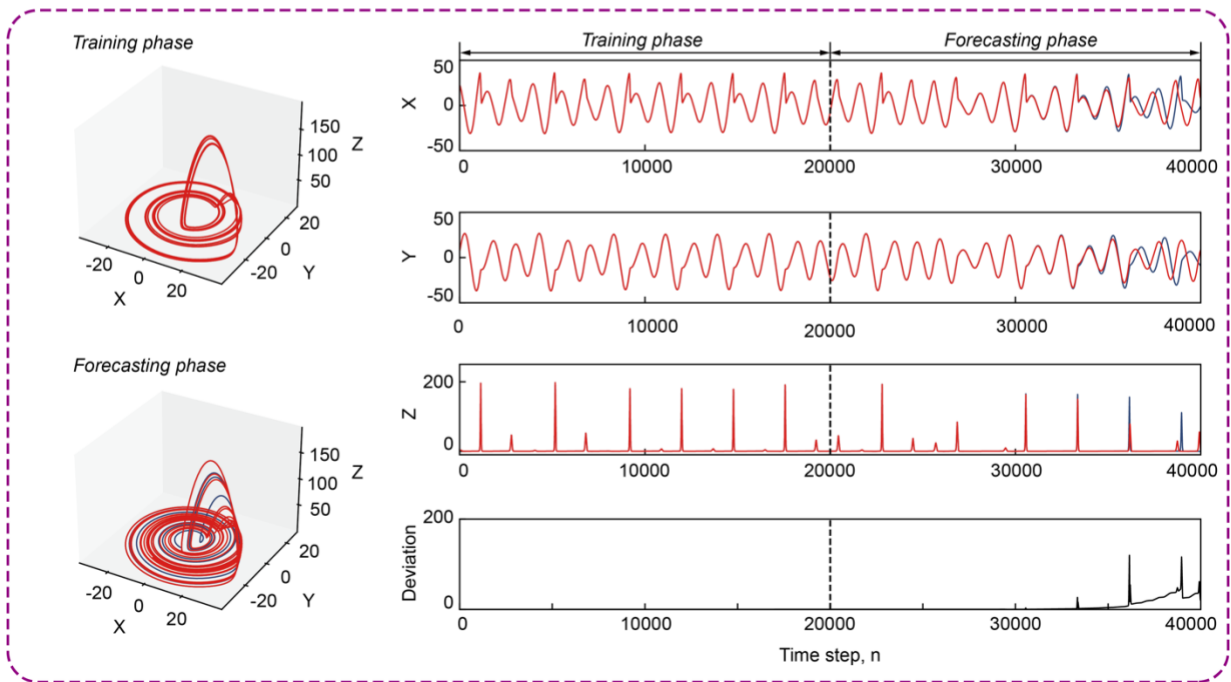
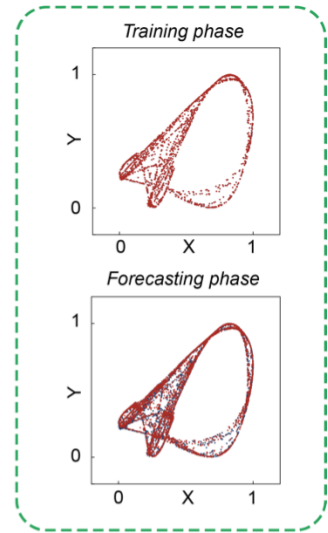


Figure S3. Maximal *Lyapunov* exponent (MLE) analysis. The MLE of dynamical systems with different dimensions and the corresponding ESN forecasting results. The target systems – (a) Mackey-Glass (1D dynamical system), (b) 2D logistic (1D dynamical system), and (c) Rössler (3D dynamical system). ESN perfectly estimates the MLE of these three different systems with the different dimensions.

1D dynamical system: Logistic map



2D dynamical system: 2D logistic map

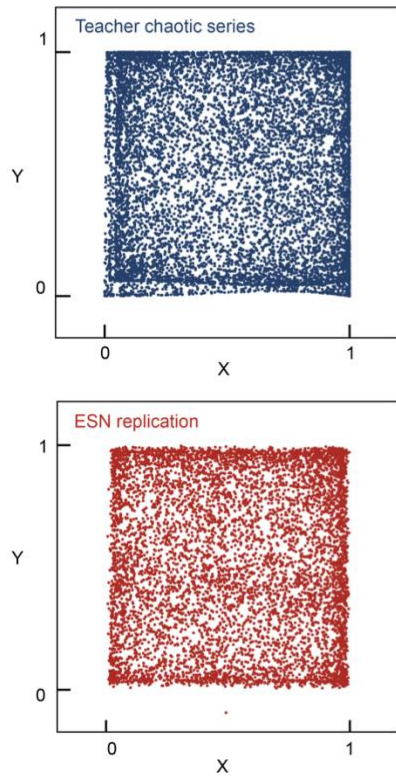


3D dynamical system: Rössler system

— Ground truth — ESN output — Deviation

Figure S4. Performance of ESN with different dimensional dynamical systems. ESN shows good performance in reconstructing and predicting the chaotic dynamics of these dynamical systems with different dimensions.

(a) Comparison between the teacher system and the ESN replication result



(b) Encryption of image with AES-ECB

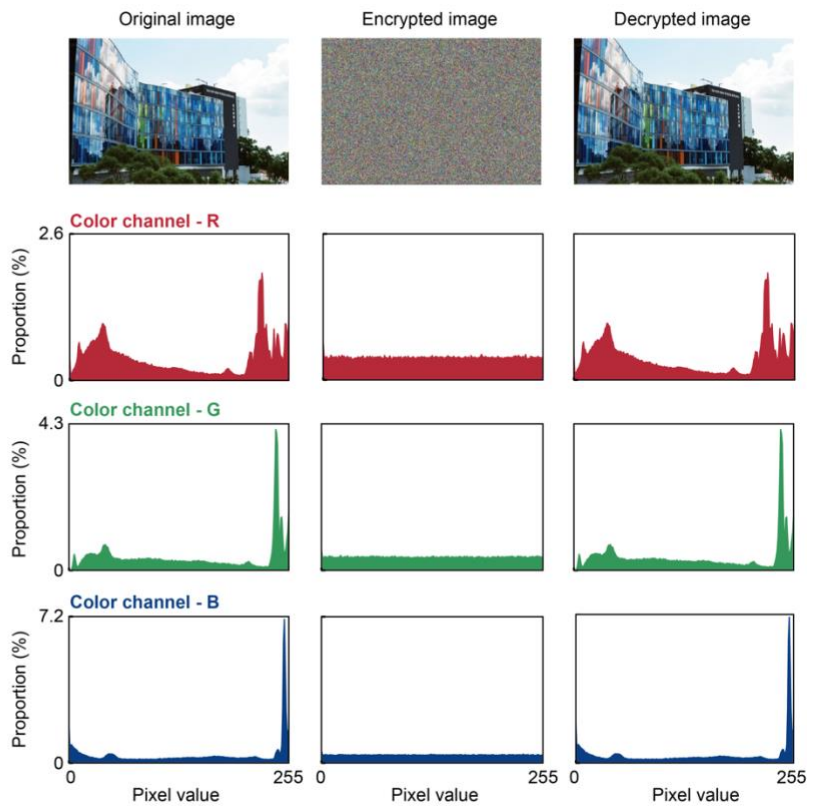


Figure S5. Data encryption using the random numbers generated by ESN. (a) Comparison in the phase portrait between the teacher system, a 2D chaotic system (upper plot), and the ESN (lower plot). (b) Image encryption using the random numbers generated by ESN. The encryption algorithm used is AES-ECB.

Supplementary Table

Table S1. Chaotica time series approximation and forecasting results by ESN.

<i>System</i>	<i>Equations</i>	<i>Origin</i>	<i>Parameters</i>	Δt	λ	λ_{ESN}
<i>Mackey-Glass</i>	$\dot{x} = \frac{b \cdot x(t - \tau)}{1 + x(t - \tau)^a} - c \cdot x(t)$	$x = 0.5$	$a = 12$ $b = 0.3$ $c = 0.2$ $\tau = 21$	1	8.595×10^{-3}	8.506×10^{-3}
<i>2D logistic</i>	$x_{n+1} = r(3y_n + 1)x_n(1 - x_n)$ $y_{n+1} = r(3x_{n+1} + 1)y_n(1 - y_n)$	$x = 0.89$ $y = 0.33$	$r = 1.19$	1	0.337	0.339
<i>Rössler</i>	$\dot{x} = -y - z$ $\dot{y} = x + ay$ $\dot{z} = b + z(x - c)$	$x = 0.1$ $y = 0.1$ $z = 0.1$	$a = 0.2$ $b = 0.2$ $c = 20$	0.005	0.187	0.179
<i>Lorenz-63</i>	$\dot{x} = a(y - x)$ $\dot{y} = x(b - z) - y$ $\dot{z} = xy - cz$	$x = 3$ $y = 2$ $z = 16$	$a = 10$ $b = 28$ $c = 8/3$	0.01	1.166	1.168

Reference

[1] Liu, S., et al. Conduction Modulation of Solution-Processed 2D Materials. *Adv. Electron. Mater.* (2024).